

## Investigation of stable dielectric permittivity with superior EMI shielding capabilities of a multifunctional NiFe<sub>2</sub>O<sub>4</sub>@MoS<sub>2</sub> nanomaterial

U. Anwar <sup>a,\*</sup>, M. Rafi <sup>b</sup>, N. A. Noor <sup>c</sup>, S. Mumtaz <sup>d\*</sup>, Hosam O. Elansary <sup>e</sup>

<sup>a</sup>*Institute of Chemical Sciences, Bahauddin Zakariya University, Multan 60000, Pakistan*

<sup>b</sup>*Department of Physics, University of Wah, Quaid Avenue, Wah Cantt 47040, Pakistan*

<sup>c</sup>*Department of Physics, University of Sargodha, 40100, Sargodha, Pakistan*

<sup>d</sup>*Department of Chemical and Biological Engineering, Gachon University, 1342 Seongnamdaero, Sujeong-gu, Seongnam-si 13120, Republic of Korea.*

<sup>e</sup>*Department of Plant Production, College of Food & Agricultural Sciences, King Saud University, P.O. Box 2460, Riyadh 11451, Saudi Arabia.*

This study presents a multifunctional NiFe<sub>2</sub>O<sub>4</sub>@MoS<sub>2</sub> nanomaterial synthesized by co-precipitation and hydrothermal methods. The highly magnified Field emission scanning electron microscopic (FESEM) images expose an excellent interconnected network of MoS<sub>2</sub> petals and NiFe<sub>2</sub>O<sub>4</sub> cores. NiFe<sub>2</sub>O<sub>4</sub>@MoS<sub>2</sub> nanomaterial's crystalline arrangement and phase purity are explored using X-ray diffraction (XRD) analysis. A comprehensive analysis of the NiFe<sub>2</sub>O<sub>4</sub>@MoS<sub>2</sub> nanomaterial, focusing on its dynamic electrical properties across a temperature zone of 183 K to 373 K. The temperature-dependent impedance and modulus plots versus frequency reveal insights into the material's conduction and relaxation. Electrical characteristics verify the contribution of electroactive regions, such as grains and surfaces, by the use of impedance spectroscopy. An analogous circuit model is used to measure different electrical characteristics. Using an adiabatic small polaron hopping model, the activation energies of bulk (0.32 eV) and various cations (0.30 eV) are estimated. Using Mott's variable range hopping model, the hopping length at the interface is calculated to be between 1.8 and 1.5 Å. Stable dielectric permittivity is explained on the basis of the polarizability of the cations and tangent loss. The NiFe<sub>2</sub>O<sub>4</sub>@MoS<sub>2</sub> nanomaterial showcases total electromagnetic interference (EMI) shielding effectiveness of 30.6 dBs around the 11GHz frequency range with a thickness of 3 mm.

(Received January 1, 2025; Accepted April 4, 2025)

**Keywords:** EMI shielding, Dielectric constant, Hydrothermal impedance spectroscopy, Co-precipitation method, Nickel ferrite nanomaterial

### 1. Introduction

The combination of EMI shielding effectiveness with dielectric stability in one material is a novel development with significant potential for multiple industries [1]. The requirement for materials that can offer strong electromagnetic interference (EMI) shielding and stable dielectric characteristics at the same time is one of the most demanding challenges facing the electronics and telecommunications industries [2]. Stable dielectric permittivity ensures consistent electrical performance, which is necessary for the reliability of transducers, capacitors and other components in high-frequency circuits [3]. Effective EMI shielding, on the other hand, is necessary to protect delicate electronic devices from outside electromagnetic disturbances, which can lead to malfunctions and poor performance [4]. Device structural design becomes simpler when these features can be combined into a single material system, which also improves the overall durability and efficiency of the designs [5]. Nanomaterials made of NiFe<sub>2</sub>O<sub>4</sub>@MoS<sub>2</sub> offer an innovative way

---

\* Corresponding author: [sohail38@gachon.ac.kr](mailto:sohail38@gachon.ac.kr)  
<https://doi.org/10.15251/CL.2025.224.293>

to overcome these difficulties [6]. The inherent ferromagnetic capabilities of nickel ferrite and the semiconducting qualities of MoS<sub>2</sub> combine to form a special hybrid structure with complementary functions [7]. It is anticipated that this combination will produce a material with improved EMI shielding capabilities and the ability to retain its dielectric characteristics throughout a wide frequency range and environmental conditions [8].

The synergistic properties of the two metals have provided development to significant physical and chemical properties that are advantageous for nanoscale spinel ferrite particles [9]. The metallic cations M<sup>2+</sup> and Fe<sup>3+</sup> can reside in octahedral and tetrahedral positions in the spinel ferrites of MFe<sub>2</sub>O<sub>4</sub> [10]. The spinel ferrite is an inverse spinel if the M<sup>2+</sup> cations are not occupying tetrahedral sublattices in the cubic closed-packed O<sup>2-</sup> lattice [11]. The ferrite is a mixed spinel if M<sup>2+</sup> and Fe<sup>3+</sup> cations are present in both sublattices [12]. The appearances of spinel, with their catalytic activity, conductivity, and magnetic behavior are noticeably obstructed by the cation possession at these locations [13]. Among them is nickel ferrite (NiFe<sub>2</sub>O<sub>4</sub>), which has intriguing electromagnetic and magnetic characteristics [14]. Chemical stability, chemical hardness, electrical resistivity, low coercivity, high saturation magnetization, and affordable price characterize the soft ferrite NiFe<sub>2</sub>O<sub>4</sub>. Due to these factors, it is used extensively as a superior material for electrical gadgets, magnetic recording medium, and magnetic resonance imaging improvement [15].

In general, MoS<sub>2</sub> nanosheets have been extensively researched in a variety of disciplines recently, including drug administration, electrocatalysts, sensors and energy storage. They are an intensifying star in two-dimensional (2D) structures [16]. Because of the quantum confinement effect, 2D MoS<sub>2</sub> is a p-type semiconductor with a straight band gap of 1.9 eV [17]. This property makes it a promising material for photocatalytic applications [18]. Furthermore, the great thermal stability and huge surface area of 2D MoS<sub>2</sub> make it a good choice for usage as a matrix to lead to additional nanomaterials [19]. NiFe<sub>2</sub>O<sub>4</sub>, a promising n-type semiconductor, has garnered a lot of consideration lately due to its stable physical and chemical properties and strong light absorption capacity [20]. Furthermore, the inclusion of NiFe<sub>2</sub>O<sub>4</sub> gives photocatalysts high catalytic recyclability and magnetic separability [21]. The creative combination of NiFe<sub>2</sub>O<sub>4</sub> and MoS<sub>2</sub> not only overcomes present constraints in EMI shielding and dielectric materials but also creates new opportunities for multifunctional nanomaterials. These nanomaterials can be customized for particular uses, where stable dielectric characteristics and efficient EMI shielding are essential, including flexible electronics, wearable technology, and aircraft components. Furthermore, NiFe<sub>2</sub>O<sub>4</sub>@MoS<sub>2</sub> nanoparticles are very appealing for commercial applications due to their environmentally friendly synthesis pathways and large-scale production capability as well as steady chemical and physical qualities [22].

The conductive composites composed of NiFe<sub>2</sub>O<sub>4</sub> modified by MoS<sub>2</sub> exhibit, a large diameter, mechanical strength, high aspect ratio and strong conductivity making them an excellent option for EMI shielding material at low filling [23]. Ferrites are good dielectric materials that can be used to increase the scattering properties of nanomaterial, thus enabling electromagnetic shielding (EMS) to be tuned across a broad frequency range. The electrical properties of spinel ferrite are largely dependent on the particle size, built-up processes, annealing temperature, shape and dispersal of cations at tetrahedral and octahedral sites [24]. Ferrites' conduction mechanism differs greatly from semiconductors. Temperature-dependent mobility in ferrites affects conductivity, although temperature variations largely do not affect the material's carrier concentration [25]. Ferrites are inhomogeneous dielectric materials due to the division of some high-conducting particles by low-conducting particles. [26]. Significant information regarding the movement of localized electrical charge carriers can be obtained by analyzing the electric properties of the ferrites to understand the mechanism of their dielectric polarization [27].

This work develops a simple method to develop high-performance EM wave absorbers using a NiFe<sub>2</sub>O<sub>4</sub> nanomaterial. In this article, sophisticated procedures are used to synthesize NiFe<sub>2</sub>O<sub>4</sub>@MoS<sub>2</sub> nanomaterial, which is intended to maximize the contact between the two materials. Achieving the intended electrical and magnetic properties requires a consistent and stable MoS<sub>2</sub> coating on NiFe<sub>2</sub>O<sub>4</sub> nanoparticles. Techniques consisting of hydrothermal synthesis and co-precipitation processes are used to carefully control the morphology and chemical composition of the nanomaterials, improving the EMI performance characteristics. Correlating dielectric qualities with electro-active regions throughout a wide temperature and frequency range will be made easier

with a thorough understanding of the electrical properties. Impedance spectroscopy (IS), the most active and popular approach to research transport mechanisms through various electroactive regions (grains, grain borders, interfaces, and contact effect), is used to explore the electrical aspects of solid-state composite systems. To isolate the contribution of each electrical region at a chosen frequency range, impedance spectroscopy is utilized. To the best of our awareness, there is a dearth of research on electrical analyses of multifunctional structures based on  $\text{NiFe}_2\text{O}_4@\text{MoS}_2$ . Investigating the multifunctional  $\text{NiFe}_2\text{O}_4@\text{MoS}_2$  nanomaterial offers a viable route toward creating next-generation materials with dual EMI and dielectric shielding properties. In addition to expanding our knowledge of hybrid nanomaterials, this work paves the way for future developments in electrical device engineering and provides answers to some of the most important technological problems of our era.

## 2. Experimental section

### 2.1. Materials

The chemical reagents utilized in this study were procured from commercial suppliers. The chemicals included iron (III) nitrate nonahydrate, sodium hydroxide (NaOH), nickel nitrate hexahydrate, thiourea, ammonium molybdate, ethanol and deionized water (DI).

### 2.2. Preparation of $\text{NiFe}_2\text{O}_4$ nanomaterial

For the preparation of multifunctional  $\text{NiFe}_2\text{O}_4$  nanomaterial via the co-precipitation method, 0.2M iron (III) nitrate nonahydrate and 0.1M nickel nitrate hexahydrate are mixed and stirred for 60 minutes and heated at  $70^\circ\text{C}$ . Then 2M solution of sodium hydroxide in 100 mL is prepared and added dropwise to the previous solution to obtain precipitates. As soon as the first drop of NaOH solution entered the salt solution, the shade of the solution turned brown and precipitates began to form. To complete the precipitate growth, the solution was agitated for one hour at  $80^\circ\text{C}$  and then for twenty-four hours at  $30^\circ\text{C}$ . After that, stirring was stopped and precipitation was allowed to settle. The precipitates are washed out numerous spells with DI water and ethanol and desiccated out the precipitated at  $70^\circ\text{C}$ . After these dried precipitates are calcined at  $600^\circ\text{C}$  for 4.5 hours in the furnace. A mortar and pestle are used to homogenize the powder when it has cooled, resulting in the ideal multifunctional nickel ferrites nanomaterial [4]. The entire process is explained in Fig.1 (a).

### 2.3. Preparation of $\text{NiFe}_2\text{O}_4/\text{MoS}_2$

In this process, 100 ml of deionized water is used to dissolve 2.3 grams of ammonium molybdate and 15.1 grams of thiourea. Brownish  $\text{NiFe}_2\text{O}_4$  powder is subsequently mixed with this solution. Subsequently, the mixture is moved to a 100 mL Teflon autoclave and heated to  $200^\circ\text{C}$  for an entire day. After being repeatedly rinsed with ethanol and DI water, the resultant black precipitates ( $\text{NiFe}_2\text{O}_4@\text{MoS}_2$ ) are desiccated at  $40^\circ\text{C}$  [28]. The entire process is explained in Fig.1 (b).

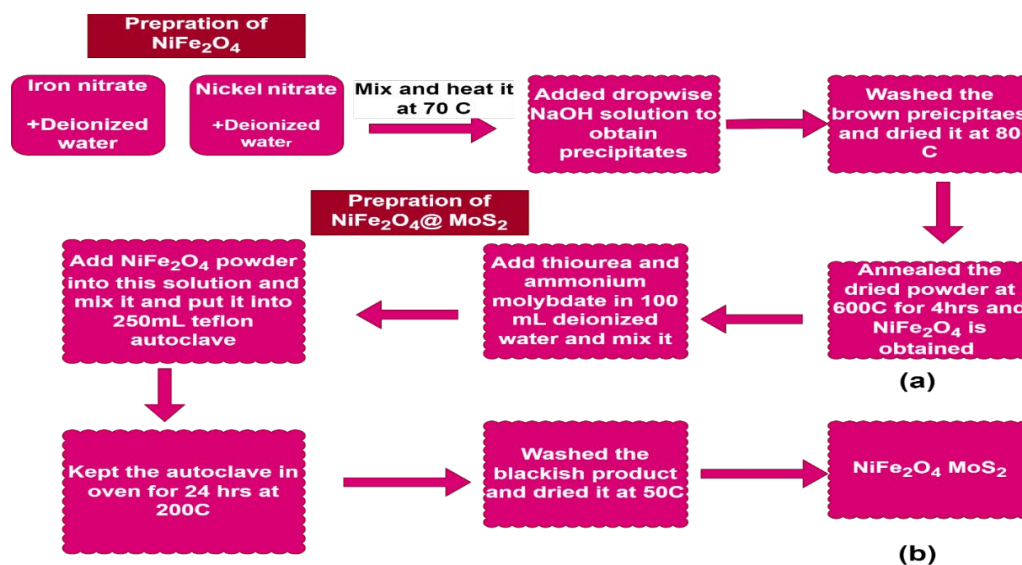


Fig. 1. Pictorial representation of Co-precipitation (a) and hydrothermal processes (b).

Using  $\text{CuK}\alpha$  radiation, the crystallite dimension and phase analysis of  $\text{NiFe}_2\text{O}_4@\text{MoS}_2$  nanomaterial is measured with (ARL EQUINOX 3000) at an examining speed of  $4 \text{ min}^{-1}$  and a step size of 0.03. Using field emission scanning electron microscopy (FE-SEM), the nano-structures and morphologies are examined. WINDETA software and Dielectric Analyzer are used for temperature and frequency-dependent impedance spectroscopy measurements, respectively. After the powder was compressed with a hydraulic press set to 5 tons of pressure for a minute, a pellet with a width of 10 mm and a breadth of roughly 2 mm was created. After thoroughly cleaning the pellet on both sides, the grey paste was used to ensure decent ohmic links. Through dielectric the AC electrical characteristics were investigated across a wide frequency range of (1Hz- $10^7$ Hz) under the temperature range of 183-373K. A very small AC signal of 0.2V was applied for each of these measurements within the specified temperature zone. A pellet-filled homemade sample holder was put inside a Dewar filled with liquid nitrogen. Moreover, a DC power supply has been used to maintain the sample's temperature. The dispersive impact of leads was thoroughly examined to prevent any unnecessary capacitive and inductive coupling. Ten minutes were spent stabilizing the temperature before collecting the impedance data for each experiment. A waveguide Vector Network Analyzer is employed for the quantity of the shielding efficiency. The ready materials are rumbled into small pieces and evenly joined with wax at a mass ratio of 1:1 before shaping into a slab size measuring  $22.5 \text{ mm} \times 10.1 \text{ mm}$  in order to examine the effectiveness of EMI shielding.

### 3. Results and discussion

FE-SEM analysis reveals the detailed morphology of the synthesized  $\text{NiFe}_2\text{O}_4@\text{MoS}_2$  nanocomposite, consistent with the expected structural characteristics based on the synthesis process. The FE-SEM images, as shown in Fig. 2, highlight the nanomaterial's peculiar flower-like structures, a characteristic that emphasizes the integration of  $\text{MoS}_2$  sheets onto the  $\text{NiFe}_2\text{O}_4$  core. Petal-like  $\text{MoS}_2$  layers dispersal from the core of the  $\text{NiFe}_2\text{O}_4$  nanoparticles provide the vast surface area design of these flower-like formations. [9]. This stacked nano-petal-like morphology has functional significance and the increased surface area improves the material's capacity to interact with electromagnetic waves, improving its dielectric stability and EMI shielding properties. Significant aggregations in the  $\text{NiFe}_2\text{O}_4@\text{MoS}_2$  nanomaterial may be related to  $\text{MoS}_2$ 's high surface adsorption.  $\text{MoS}_2$  nanosheets, demonstrating the robust interfacial contact. The consistent and homogenous  $\text{MoS}_2$  coating on the  $\text{NiFe}_2\text{O}_4$  particles appears in the high-resolution FESEM pictures, which point to a meticulously controlled synthesis process.  $\text{MoS}_2$  petals appear to be thin and

uniformly distributed, which improves the nanomaterial's overall structural stability.  $\text{NiFe}_2\text{O}_4$  nanoparticles can be dispersed more effectively in this flower-like structure, which reduces agglomeration and guarantees uniform material characteristics throughout the composite. The enhanced surface area of the  $\text{NiFe}_2\text{O}_4@\text{MoS}_2$  nanomaterial is expected to improve its interaction with electromagnetic waves, leading to improved dielectric stability and EMI shielding effectiveness, making the observed shape functionally significant. The strong surface adsorption characteristics of  $\text{MoS}_2$  layered structured coating, which support significant interfacial contact between components, might be the cause of the observed aggregations of  $\text{NiFe}_2\text{O}_4@\text{MoS}_2$  nanocomposites. One possible explanation for the inconsistencies in surface coverage is the partial or uneven  $\text{MoS}_2$  deposition onto the  $\text{NiFe}_2\text{O}_4$  nanoparticle's surface. This can cause non-uniform growth of  $\text{MoS}_2$ , giving the appearance of being non-homogeneous in places where better nucleation and deposition occur but not in others. The observed morphology may also be explained by variables like the aggregation of nanoparticles during synthesis and the different particle size distributions of  $\text{NiFe}_2\text{O}_4$  nanoparticles.

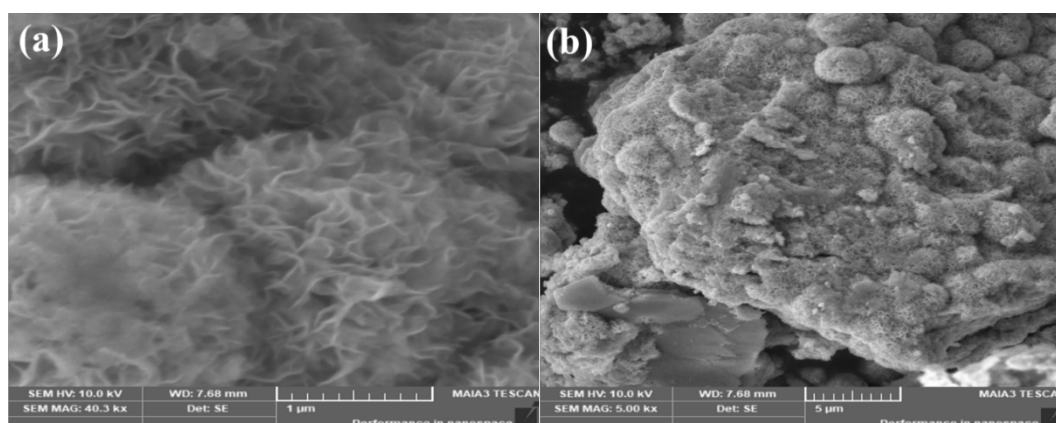


Fig. 2. (a, b) Signifies the FE-SEM image of  $\text{NiFe}_2\text{O}_4@\text{MoS}_2$  nanomaterial at 40000x and 5000x.

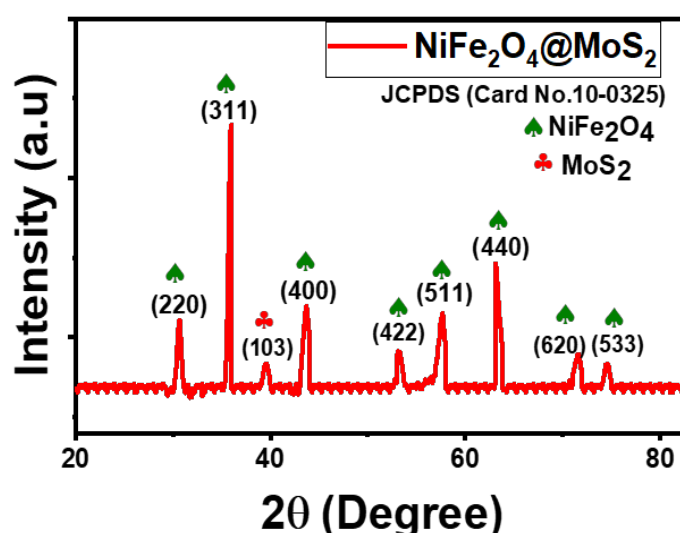


Fig. 3. Represents the X-ray diffraction pattern (XRD) of  $\text{NiFe}_2\text{O}_4@\text{MoS}_2$  nanomaterial.

The synthesized  $\text{NiFe}_2\text{O}_4@\text{MoS}_2$  nanomaterial's crystalline morphology and phase integrity were explored using XRD analysis. Fig. 3 represents the XRD pattern clear diffraction peaks for both  $\text{MoS}_2$  and  $\text{NiFe}_2\text{O}_4$ , indicating that the hybrid nanomaterial successfully formed. The  $\text{NiFe}_2\text{O}_4$

cubic spinel structure reflections (220), (311), (222), (400), (422), (511), (440), (620), and (533) can appear in the XRD patterns at  $2\theta = 30.2^\circ, 35.6^\circ, 37.4^\circ, 43.4^\circ, 48.6^\circ, 57.0^\circ, 63.2^\circ, 69.0^\circ,$  and  $74.6^\circ$ . The standard JCPDS (Joint Committee on Powder Diffraction Standards) cards for  $\text{NiFe}_2\text{O}_4$  and  $\text{MoS}_2$  can be utilized to calculate the precise diffraction angles for these planes in the  $\text{NiFe}_2\text{O}_4@/\text{MoS}_2$  nanocomposite. The cubic spinel structure of  $\text{NiFe}_2\text{O}_4$  (nickel ferrite) nanoparticles is generally characterized by its XRD peak positions. With  $\text{Cu-K}\alpha$  radiation ( $\lambda=1.54\text{\AA}$ ), the following  $2\theta$  values are typically where the significant peaks for  $\text{NiFe}_2\text{O}_4$  are observed. The peaks found in  $\text{NiFe}_2\text{O}_4@/\text{MoS}_2$  and the ICSD reference number 00-010-0325 match as well.  $(\text{Fe}^{3+})_A[\text{Ni}^{2+}\text{Fe}^{3+}]_B\text{O}_2^{-4}$  is the crystalline structure of  $\text{NiFe}_2\text{O}_4$  with atomic occupancy, where A and B represent tetrahedral and octahedral sites in the spinel structure, respectively. nanoparticles, reducing the likelihood of agglomeration and guaranteeing uniform material characteristics across the composite [29]. Simultaneously, the distinctive peak of  $\text{MoS}_2$ , detected at  $39.5^\circ$  aligns with the (103) plane, under  $\text{MoS}_2$ 's hexagonal structure (JCPDS card no. 37-1492). These peaks are prominent, indicating that the  $\text{MoS}_2$  layers are well-organized and retain their crystalline structure when integrating with  $\text{NiFe}_2\text{O}_4$  [18]. The calculated average crystallite size of  $\text{NiFe}_2\text{O}_4@/\text{MoS}_2$  from the highest diffraction peak by the Debye-Scherrer formula ( $D = 0.9\lambda / \beta\cos\theta$ ) is 24 nm.

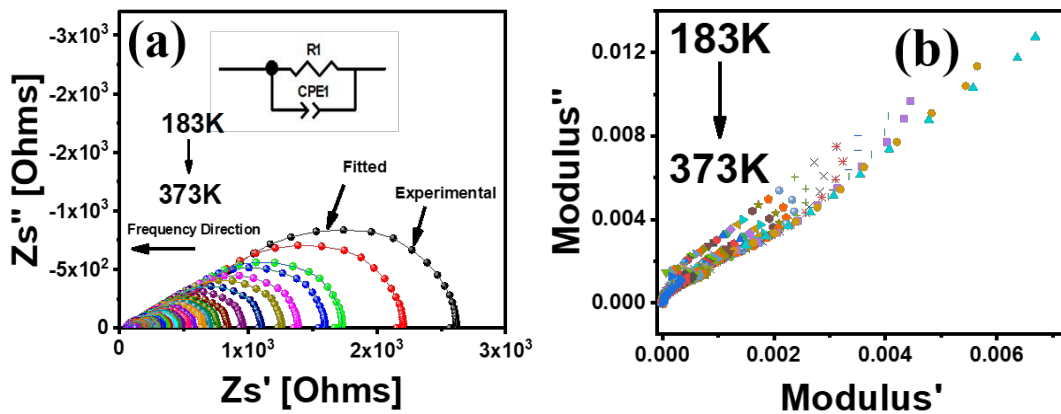


Fig. 4. (a), (b) shows impedance and modulus plane plots of  $\text{NiFe}_2\text{O}_4@/\text{MoS}_2$  nanomaterial at 183 K-373 K temperatures at (1Hz-10MHz) frequency ranges, and the ramp rate used during the experiments is  $2^\circ\text{C}/\text{min}$ .

Impedance spectroscopy is employed to examine the impedance plane plot of the nanomaterial over a temperature range of 183 K to 373 K. ZView software is used to fit an equivalent circuit model to the experimental impedance data to gain an inclusive understanding of the electrical features of the  $\text{NiFe}_2\text{O}_4@/\text{MoS}_2$  nanomaterial. The model ( $R_1Q_1$ ), as illustrated in the inset of Fig. 4 (a), accurately represents the complex impedance behavior of the nanomaterial material. It consists of one resistance ( $R_1$ ), and one constant phase element (CPE). The impedance fitting study yields excellent goodness-of-fit (GoF) with fitting parameter values within a 3–4% error [30]. Table 1 presents the values of close-fitting parameters for the equivalent circuit model. The temperature range is increased from the top (low-temperature ranges (183K)) to the bottom (high-temperature ranges (373K)) as indicated by the direction of the arrow.

Table 1. Summary of fitted parameters of circuit model ( $R_1Q_1$ ) for  $\text{NiFe}_2\text{O}_4@\text{MoS}_2$  in Zview at some selective temperature. (Updated whole fitted parameters based on equivalent circuit model).

T(K)	$R_1(\Omega)$	Q	n
183	2668	$2.19 \times 10^{-9}$	0.77
203	1455	$3.27 \times 10^{-9}$	0.71
253	994	$3.21 \times 10^{-9}$	0.68
303	449	$1.22 \times 10^{-9}$	0.61
333	240	$1.21 \times 10^{-8}$	0.57
363	140	$3.02 \times 10^{-8}$	0.54

A depressed semicircular arc present at low to high-frequency region in the impedance plane plot at a temperature zone of (183K-373K) represents the bulk resistance ( $R_1$ ) associated with the  $\text{NiFe}_2\text{O}_4$  core and  $\text{MoS}_2$  layers. This arc represents the fundamental characteristics of the grain, wherein the electroactive charge carriers move across the crystalline lattice. The diameter of the semicircle indicates the resistance within the grains and, hence, the ease of activated electron mobility in the bulk material. Additionally, it is significant to note that the temperature zone affects the diameter of the depressed semicircular arc [31]. As exemplified in Fig. 4 (a), the occurrence of a single semicircular arc in the impedance plane plot specifies the existence of a vast relaxation process, which is categorized by a noteworthy relaxation time ( $\tau = RC$ ). Here, R,  $\tau$  and C stand for the resistance, relaxation time and capacitance corresponding to the charge carriers in the broad relaxation process [32]. The frequency progression from the low to the high section is depicted by the arrows. The structure of these arcs varies with temperature, indicating a change in the capacitive and resistive properties of the material. Electroactive charge carrier mobility is directly correlated with the relaxation frequency, which assesses how quickly charge carriers respond to variations in the applied AC electric field.

The CPE explains the non-ideal, frequency-dependent capacitance behavior commonly observed in heterogeneous materials, like this nanomaterial, where the relaxation periods are distributed. As the temperature increases to 373 K, the impedance graphs clearly demonstrate a reduction in the linear tail's slope and the semicircle's breadth. Increased thermally activation of charge carriers causes a drop in bulk resistances ( $R_1$ ), which explains this shift in the conduction mechanism. The total impedance decreases as a result of higher temperatures, which provide charge carriers greater energy to get past possible obstacles. This temperature-dependent behavior is consistent with the usual conduction mechanisms in ferrite-based nanomaterial, where a higher temperature causes electron hopping to occur more easily and grain boundary obstacles to have less of an effect. The study gains further depth by incorporating the constant phase element (CPE) into the equivalent circuit model, which accounts for the non-ideal capacitive responses and widespread relaxation phenomena found in the experimental data. This nanomaterial is especially important for precisely simulating the behavior of impedance across a broad frequency range, guaranteeing that the intricate interaction between bulk and interfacial effects is completely represented.

The analysis of the modulus plane plot of the  $\text{NiFe}_2\text{O}_4@\text{MoS}_2$  nanomaterial, performed over a temperature ranges of 183 K to 373 K, provides detailed information about the dielectric relaxation and electrical properties of the material, as illustrated in Fig. 4 (b). The modulus plane plot, which highlights the bulk properties of the material by attenuating the effects of electrode polarization, provides a clearer image of the intrinsic electrical behavior and relaxation phenomena within the composite [33]. The modulus plane plot is conquered at lower temperatures, about 183 K, by a single relaxation process that is consistent with the dipolar relaxation occurring within the  $\text{MoS}_2$  layers and  $\text{NiFe}_2\text{O}_4$  cores, where the flexibility is restricted and the charge carriers are focused. [34]. The modulus peaks move towards higher frequencies and get smaller in amplitude as the temperature rises to 373 K. This change indicates that the relaxation time has decreased, pointing to faster dipolar relaxation processes at higher temperatures. The lower peak height indicates increased mobility of charge carriers since the heat energy makes it easier for the carriers to get through obstacles and accelerates the polarization and depolarization cycles [35]. The substantial temperature dependency of the material's dielectric characteristics is also evident in the modulus plane plot. The patterns that

have been observed indicate that thermally triggered processes are primarily responsible for the dielectric relaxation of the nanomaterial. These activities improve the dielectric response overall and help explain the material's exceptional performance throughout a wide temperature range [36].

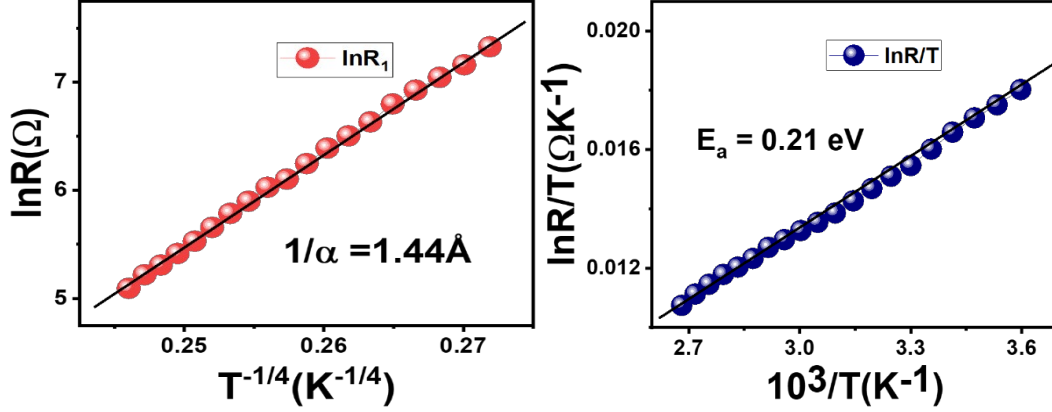


Fig. 5. (a) To assess the confinement length, the Mott variable range hopping (VRH) model is utilized (b) Employing a small polaron hopping model, the activation energies of electroactive charge carriers moving through the bulk, interface, and grains are measured.

Using an analogous circuit model approach, the conduction process is explicated by utilizing the resistance ( $R_1$ ) within the electro-active zone. In the temperature range of 183 K to 373 K, we employed the MVRH model in conjunction with the SPH model for our analysis.

Expression for MVRH model.

$$\ln(\rho/\rho_0) = (T_0/T)^{1/4} \quad (1)$$

where  $T_0$  is Mott's representative temperature and  $\rho_0$  is the resistivity's high-temperature limit. The equation for the aforementioned  $\rho(T)$  expression is as follows:

$$\rho = \rho_0 \exp [2.06(\alpha^3/N(E) kT)^{1/4}] \quad (2)$$

That is the Mott expression:

$$kT_0 = 18 \alpha^3/N(E) \quad (3)$$

The density of phases is signified by  $N(E)$  in this equation respectively, while the inverse of the localization length is  $\alpha$ . A physically little value of the localization length  $1/\alpha$  is attained by employing the entire value of the  $e_g$  electron density in the density of states.

With these concerns, the equation yields:

$$kT_0 = 171 \alpha^3 U_m \nu \quad (4)$$

where  $\nu$  is the lattice volume per iron ion ( $0.54 \times 10^{-29} \text{ m}^3$ ) and  $U_m$  is the magnetic potential magnitude. The majority of hopping occurrences take place between points whose energies fall into a specific range. As seen in Fig. 5 (a), the resistance ( $R_1$ ) is graphed alongside the inverse of temperature over the temperature zone of 183 K to 373 K using the MVRH model [28]. The fitted parameters from the related circuit are utilized for this illustration. The  $\text{NiFe}_2\text{O}_4@\text{MoS}_2$  nanomaterial's hopping carrier localization length is determined to be  $1/\alpha = 1.44 \text{ \AA}$  following the fitting of the MVRH model. Because of the stochastic variations in potential, at low temperatures, the electroactive charge carriers are more prospective to take part in bouncing proceedings with activation energies that are more extensively parted from their nearby neighbors. The hopping

probability between localized states is closely related to the localization length, a characteristic that characterizes the dispersion of an electron wave function in a disordered system. The localization length (1.44 Å) results suggest that the charge carriers are somewhat limited in these localized sites, requiring thermal activation to hop between localized sites. The confinement seen in the NiFe<sub>2</sub>O<sub>4</sub>@MoS<sub>2</sub> nanomaterial is characteristic of materials exhibiting severe disorder or those consisting of many phases. In comparison to the region with a localization length of 1.44 Å, indicates a region where the electronic states are more delocalized. This difference is explicated by the intrinsic material heterogeneity, in which differing levels of electrical disorder are formed by the MoS<sub>2</sub> and NiFe<sub>2</sub>O<sub>4</sub> components. The magnetic interactions may contribute to a longer localization length by extending the electronic state in the NiFe<sub>2</sub>O<sub>4</sub>-rich regions. On the other hand, shorter localization lengths may occur in MoS<sub>2</sub>-dominated regions due to strong covalent bonding and potential structural flaws.

Expression for SPH Model.

$$\ln(\rho/T) = \ln A + W/kT \quad (5)$$

The SPH model is applied over the temperature zone of 183 K to 373 K in Fig. 5 (b). The calculated activation energy, resulting in out to be  $E_a = 0.21$  eV, offers further evidence that this combination of nanomaterials promotes polaronic conduction. At that temperature, a high number of trap insides begin to enhance the SPH paradigm by promoting effective connections among the Fe<sup>2+</sup> and Fe<sup>3+</sup> straits, acting as repositories for charge carriers. The region of the composite where the energy barriers for charge carrier movement are particularly high is correlated with the activation energy of 0.21 eV [37]. Because of the stronger electron-phonon interactions in this region, the higher activation energy indicates that the electronic states are more confined [38].

This situation is common in the NiFe<sub>2</sub>O<sub>4</sub>-rich domains, where magnetic ion concentrations and related lattice distortions lead to large potential obstacles for polaronic hopping. The increased activation energy recommends that the high-temperature conductivity performance of the composite is primarily precise by this region. Because of the lower activation energy, there may be less structural disorder or electron-phonon coupling, which would create a more conducive environment for tiny polaronic hopping. This reduced activation energy is possibly a consequence of the MoS<sub>2</sub>-dominated regions, which are illustrious by their layered structure and comparatively lower degree of lattice distortions. As a result, at lower temperatures, this area is critical to the conductivity of the composite [39].

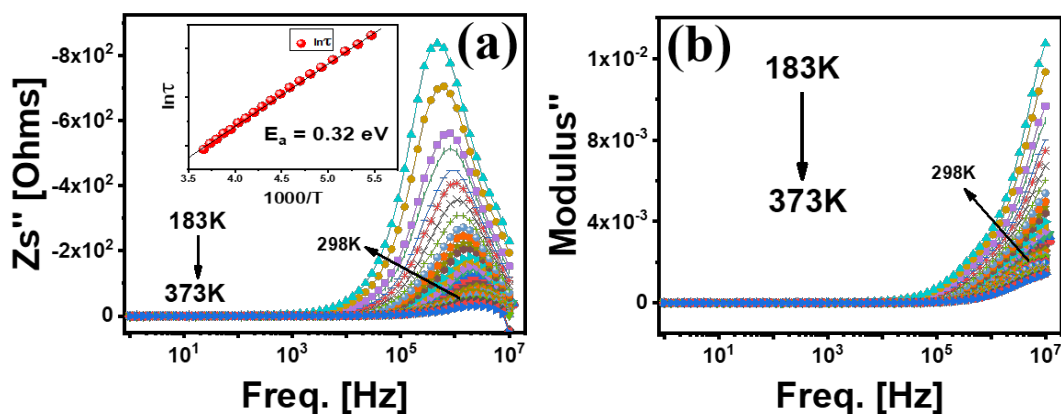


Fig. 6. (a) Bode plot of the imaginary part of Impedance ( $Z''$ ) versus frequency and (b) Electric Modulus  $M''$  versus frequency at 183K-373K.

Fig. 6 (a) shows the change in the impedance loss spectrum ( $Z''$ ) concerning the applied frequency range at different temperatures. A more pronounced asymmetric peak with a center at  $\sim 10^6$  Hz is visible at 298 K, which represents the nanomaterial's relaxation time distribution. The

observed shift of this peak toward the higher frequency side ( $f > 10^6$  Hz) and enhanced suppression of intensity with increasing temperature point to an escalation in the loss of  $Z''$  in the material. The cationic disorder of the material at lower temperatures is the cause of this phenomenon. Furthermore, the low-intensity broad peak at  $\sim 373$  K shows that space charges are building up at the interface at high temperatures.  $Z''$  values are relatively high in the low-frequency domain, suggesting large energy dissipation because resistive components predominate in the impedance [40]. This phenomenon is indicative of the significant resistance that the charge carriers are facing as they pass through the microstructure of the material. The high  $Z''$  values at low frequencies reflect the interfacial polarization, where charge accumulation at the interfaces between the  $\text{MoS}_2$  and  $\text{NiFe}_2\text{O}_4$  layers contributes to energy loss. The Bode plot of  $Z''$  usually exhibits a peak as the frequency increases, which indicates the composite's distinctive relaxation frequency. The activation energy is calculated to be ( $E_a = 0.32$  eV) by using the Arrhenius relation shown in the inset of Fig. 6(a) which is relatively comparable to the activation energy premeditated from the SPH model.

$\text{Ni}^{2+}$  dopant cations occupy octahedral symmetry sites, resulting in the formation of oxygen vacancies and inherent defects. The bode plot modulus ( $M''$ ) in the specified temperature zone (183–373 K) is shown in Fig. 6 (b). The value of  $M''$  on the left-hand side (at low frequency  $< 10^3$  Hz) in Fig. 6 (b) is independent of frequency. Because long-range electroactive charge carrier's mobility or electrode polarization effects predominate at low frequencies, the imaginary component of the electric modulus  $M''$  tends to stay relatively constant. Ionic and dipolar relaxations have less effect in these frequency zones because the charges and dipoles have adequate time to fully react to the alternating electric field. The polarization mechanisms eventually approach equilibrium, which results in the frequency-independent behavior of  $\text{NiFe}_2\text{O}_4@/\text{MoS}_2$  nanomaterials that has been seen in the modulus plot. The system acts as though it has adequate time to let charge accumulation or drift in this frequency range, which slows down the relaxation processes ( $\tau$ ) and lessens the frequency dependency of the imaginary part of the modulus ( $M''$ ). The low-frequency region's constant  $M''$  is commonly associated with electrode polarization, a phenomenon in which charges build up at the electrode-sample interface instead of being subjected to bulk relaxation mechanisms [41]. The activation energy for  $Z''$  is computed using equations (6) and (7), and the result is 0.32 eV, as seen in the inset of Fig. 6 (a). The energy inferred from the SPH model and the activation energy recovered from peak frequencies (Figs. 5 (b) and 6 (a)) are pretty similar, which signifies that relaxation and conduction processes are associated with the same electroactive regions. [40].

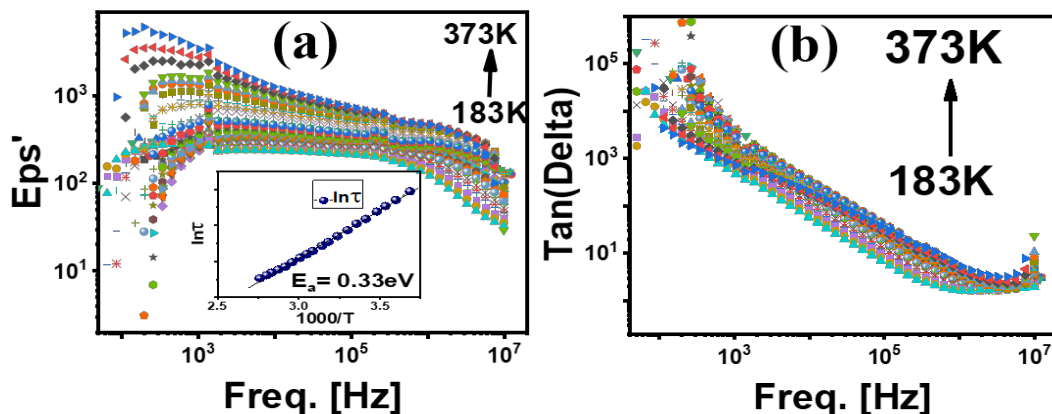


Fig. 7. (a) Dielectric constant ( $\epsilon'$ ) versus frequency (b) tangent loss ( $\tan\delta$ ) versus frequency at 183K–373K temperatures.

The reciprocation of the dielectric constant ( $\epsilon'$ ) to frequency across a wide temperature range (183 K–373 K) is shown in Fig. 7(a), which illustrates the existence of multiple types of polarization in the material. The composite is flexible against temperature variations, as seen by the stability of the dielectric constant over a broad temperature range. The high dielectric constant at lower

temperatures (183 K) suggests that the material has robust polarization mechanisms. All of these processes are most likely due to the inherent properties of NiFe<sub>2</sub>O<sub>4</sub> and MoS<sub>2</sub>, wherein the NiFe<sub>2</sub>O<sub>4</sub> core increases magnetic polarization and the MoS<sub>2</sub> layers enhance interfacial polarization. [37]. MoS<sub>2</sub>'s layered structure and NiFe<sub>2</sub>O<sub>4</sub>'s ferrimagnetic characteristics work together to effectively separate charges and align dipoles, which produces a high dielectric response [42]. Interfacial polarization at the lower frequency region between NiFe<sub>2</sub>O<sub>4</sub> nanoparticles is improved by the MoS<sub>2</sub> coating. Because MoS<sub>2</sub> has a large surface area, it forms heterogeneous interfaces with ferrite particles, assisting in the polarization of space charge. As a result, the composite's dielectric constant rises due to the interconnected channels of NiFe<sub>2</sub>O<sub>4</sub> nanoparticles along with MoS<sub>2</sub> layered structure coating. MoS<sub>2</sub> is an electronic material that is layered and has tunable characteristics. New dipolar and interfacial polarization processes are introduced by its interaction with NiFe<sub>2</sub>O<sub>4</sub>, improving the dielectric response over a broad frequency range. Particularly at higher frequencies, MoS<sub>2</sub> functions as an insulating barrier between conducting NiFe<sub>2</sub>O<sub>4</sub> particles, aiding in limiting leakage currents and lowering dielectric losses.

The dielectric constant does not change even at 373 K, indicating that the composite can withstand high temperatures without losing its polarization properties. To ensure dependable performance without appreciable dielectric loss, thermal stability is essential for applications in temperature-variable regions. The constant dielectric constant also suggests that there aren't many dielectric relaxation processes at this temperature range, indicating that the composite suppresses the dielectric dispersion-causing heat-activated dipole reorientation and charge carrier hopping effectively. The overall frequency and temperature stability of (10<sup>3</sup>), along with its high dielectric constant, can be explained by the synergistic effect of the MoS<sub>2</sub> and NiFe<sub>2</sub>O<sub>4</sub> nanomaterial. The high magnetic permeability of the NiFe<sub>2</sub>O<sub>4</sub> core and the exceptional dielectric properties of the MoS<sub>2</sub> layers combine to form a nanomaterial material that maximizes the contributions of both magnetic and dielectric forces to polarization. Higher frequencies exhibit a steady dielectric constant, suggesting that the composite can withstand alternating electric fields with little to no frequency-induced dielectric loss. Applications in capacitors, frequency-dependent devices, and dynamic random-access memory (DRAM) benefit from this behavior since they require a stable dielectric response across a range of operating frequencies [43].

Equation (6) represents the highest frequency value of tanδ and real permittivity, which correspond to the relaxation frequency (f<sub>r</sub>). The subscript 'r' and relaxation time (τ) are indicated accordingly. The dependence of temperature is as follows:

$$f_r = (2\pi\tau)^{-1} \quad (6)$$

$$\tau = \tau \exp(-E_a/KT) \quad (7)$$

The beginning of high dielectric permittivity (ε') at the low-frequency side (~10<sup>3</sup> Hz) is determined by the combined effects of defects such as vacancies and phases of NiO and Fe<sub>2</sub>O<sub>4</sub>. The equivalent activation energy intended from ε' peak frequencies is shown in the insets of Fig. 7 (a). The resultant activation energy is (0.33 eV) deduced from Eqs. (6) and (7).

According to Fig. 7(b), the NiFe<sub>2</sub>O<sub>4</sub>@MoS<sub>2</sub> nanomaterial undergoes considerable dielectric relaxation and energy loss, but it stays within acceptable bounds for many electronic applications. At higher frequencies, the tangent loss value is significantly more than 1, which indicates this. This controlled loss demonstrates the material's ability to achieve a balance between a high dielectric constant and low energy dissipation. It is possible to ascribe the somewhat greater tangent loss at the lower end of the temperature spectrum (183 K) to the inherent characteristics of the components that make up the composite [44]. The MoS<sub>2</sub> layers, with their high dielectric constant, cause dielectric losses, while the ferrimagnetic NiFe<sub>2</sub>O<sub>4</sub> component contributes to magnetic losses. Energy dissipation can result via interfacial polarization and charge carrier hopping at the interface between these two materials, which is also very important.

Table 2. Gives a brief explanation of the temperature-dependent dielectric constant ( $\epsilon'$ ) and minimum tangent loss ( $\tan\delta$ ).

Temp (K)	Dielectric Constant ( $\epsilon'$ )				Tangent Loss ( $\tan\delta$ )	
	$10^4$ (Hz)	$10^2$ (Hz)	5 (MHz)	10 (MHz)	5 (MHz)	10 (MHz)
183	232	74	44	35.2	1.8	3.1
203	252	191	64.3	45.8	1.9	2.2
248	383	210.9	130.6	84.1	1.84	2.7
308	464.2	353.4	198.3	110.1	2.2	4.6
323	6561	255	242.5	118.5	1.97	4.5
373	1886	5133	269	134.4	1.29	3.6

At reduced frequencies, the NiFe<sub>2</sub>O<sub>4</sub>@MoS<sub>2</sub> nanomaterial's conductivity shows a comparatively low and stable value, suggesting that the hopping conduction mechanism is responsible for the DC-like behavior. Charge carriers encounter significant resistance in this frequency range in Fig. 8(a), primarily due to localized states in the composite. The high resistive nature at low frequencies highlights the intrinsic properties of the material and the interfaces between MoS<sub>2</sub> and NiFe<sub>2</sub>O<sub>4</sub>, where interfacial polarization and charge trapping may occur. The conductivity begins to increase as the frequency rises, indicating the beginning of AC conductivity mechanisms [45]. This frequency-dependent conductivity increase is indicative of charge carriers' increased mobility in an alternating electric field. The relaxation processes and the release of trapped charge carriers, which start to play a major role in the overall conduction process, are responsible for the behavior of the AC conductivity. The high-frequency conductivity transition indicates the frequency at which charge carrier hopping between localized states becomes more efficient [46].

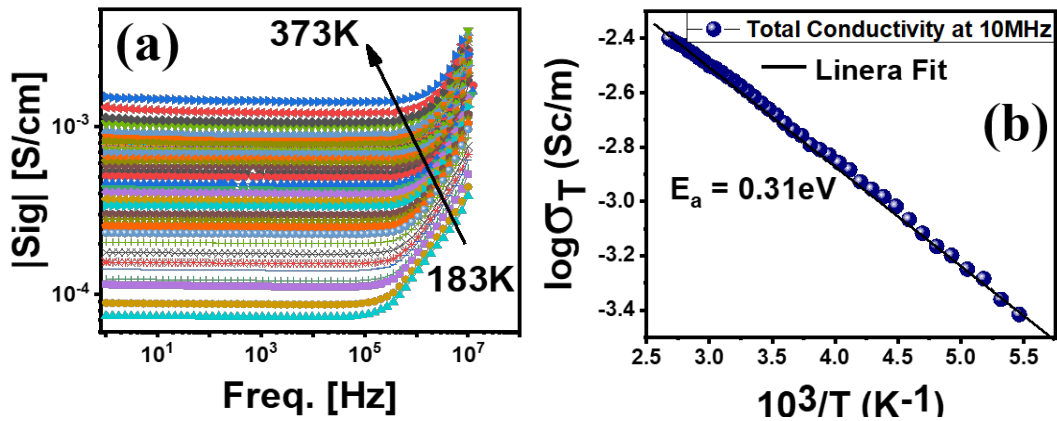


Fig. 8. (a) conductivity versus frequency, (b) total conductivity versus the inverse of temperature at 183K-373K.

The conductivity behavior can be explained by the formula  $\sigma_t = \sigma_{dc} + A\omega^s$ , where  $\sigma_t$  is the AC conductivity,  $\omega$  is the angular frequency ( $2\pi f$ ), Where A is the polarizability factor and “s” is the temperature-based exponent. Higher frequency facilitates the flow of electrons and holes between the Fe<sup>3+</sup> and Ni<sup>2+</sup> ions, which in turn increases the activity of conductive channels. Localized d electrons bouncing crosswise valence circulations of cations that normally reside in the oxygen octahedral position is a common cause of transport events in ferrites. A partition of the cation's third level produces triply degenerate t<sub>2g</sub> (more stable) electrons and doubly degenerate e<sub>g</sub> electrons (less stable). The electrostatic interaction between a cation's and an anion's electron is responsible for this splitting. Conduction in ferrites may result from the transition between Fe<sup>2+</sup> ↔ Fe<sup>3+</sup> or Ni<sup>2+</sup> ↔ Ni<sup>3+</sup> ions due to the bouncing of charge carriers among neighboring octahedral B sites. At the B site, the

conductivity is determined by the interaction between the anions (c-a-c) and the cations (c-c). Therefore, the (c-c) interactions that are promoted by the drive of atoms between the A and B sites are invariably linked to the presence of distinct metallicity [47]. The total values of conductivity for NiFe<sub>2</sub>O<sub>4</sub>@MoS<sub>2</sub> nanomaterial measured at 10 MHz for all temperature ranges are shown in Fig. 8 (b), where the solid lines best fit the Arrhenius relation. According to the SPH model, impedance, dielectric, conductivity data, and activation energy ( $E_a = 0.31$  eV) determined, that relaxation and conduction progressions are correlated with similar electro-active sections.

Using the rectangular waveguide approach (x-band), a vector network analyzer determined the overall shielding effectiveness created on the scattering parameters  $S_{11}$ ,  $S_{12}$ ,  $S_{21}$ , and  $S_{22}$ . The following is the relationship between the absorption coefficient (A), reflectance (R), and transmittance (T):

$$SE_T (\text{dB}) = SE_A + SE_R + SE_{MR} \quad (8)$$

when  $SE_A$  is less than 10 dB, the equation above can be written as follows:

$$SE_T (\text{dB}) = SE_A + SE_R \quad (9)$$

$$R = |S_{11}|^2 = |S_{22}|^2 \quad (10)$$

$$T = |S_{12}|^2 = |S_{21}|^2 \quad (11)$$

$$T + R + A = 1 \quad (12)$$

$$A = 1 - R - T \quad (13)$$

$$A_{\text{eff}} = (1 - R - T) / (1 - R) \quad (14)$$

The  $SE_R$ ,  $SE_A$ , and  $SE_T$  can be expressed as follows [28].

$$SE_A = -10 \log (1 - A_{\text{eff}}) \quad (15)$$

$$SE_R = -10 \log (1 - R) \quad (16)$$

$$SE_T = -10 \log T \quad (17)$$

The  $SE_R$ ,  $SE_A$  and  $SE_T$  values over the x-band are calculated using equations (15), (16) and (17).

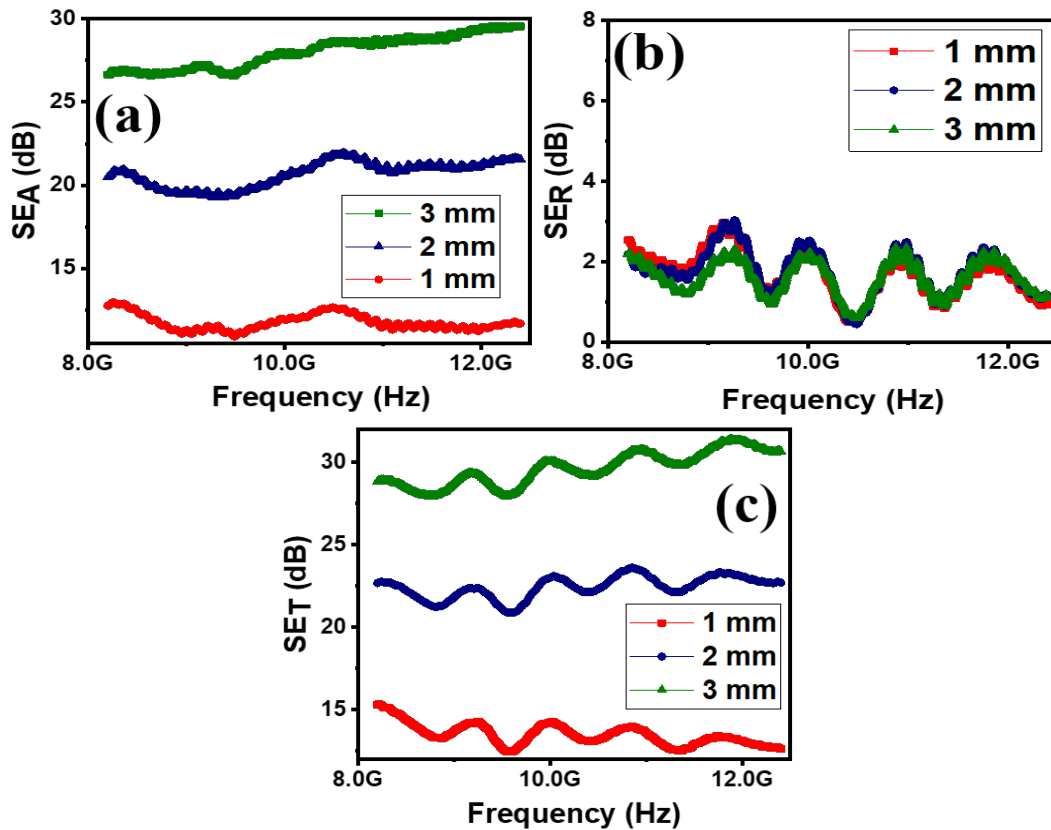


Fig. 9. Shielding effectiveness due to (a) absorption ( $SE_A$ ) (b) reflection ( $SE_R$ ) and (c) total shielding effectiveness ( $SE_T$ ).

The  $\text{NiFe}_2\text{O}_4@\text{MoS}_2$  nanomaterial exhibits remarkable electromagnetic interference (EMI) shielding effectiveness primarily due to absorption, achieving an impressive 29.6 dB across the 8–12 GHz frequency range off just 3 mm as shown in Fig. 9 (a). This high level of shielding effectiveness (SE) underscores the material's capability to attenuate electromagnetic waves through multiple mechanisms. The nano flower-like morphology of the nanomaterial, with its high surface area and hierarchical structure, plays a pivotal role in enhancing absorption. The  $\text{NiFe}_2\text{O}_4$  cores provide magnetic loss mechanisms through natural resonance and eddy current losses, while the  $\text{MoS}_2$  layers contribute to dielectric losses via interfacial polarization and dipole relaxation [48]. The synergistic interaction between the magnetic  $\text{NiFe}_2\text{O}_4$  and the semiconducting  $\text{MoS}_2$  creates numerous interfaces, facilitating the efficient dissipation of electromagnetic energy. These interfaces act as scattering centers, increasing the path length of the incident waves and enhancing multiple internal reflections within the material. Consequently, the electromagnetic energy is converted into heat through dielectric and magnetic loss mechanisms, leading to significant attenuation.  $\text{MoS}_2$  layered coatings increases the efficiency of electromagnetic interference shielding (EMI) by providing more paths for charge carrier migration and incident electromagnetic wave reflection/scattering. Inherently conducting  $\text{MoS}_2$  helps to absorb electromagnetic radiation, enhancing  $\text{NiFe}_2\text{O}_4$ 's magnetic characteristics.  $\text{MoS}_2$  increases dielectric loss while  $\text{NiFe}_2\text{O}_4$  contributes to magnetic loss. Combining the two results in an absorption-dominated shielding mechanism, which is preferable for effective electromagnetic interference shielding over reflection-dominated shielding. Because  $\text{NiFe}_2\text{O}_4$  offers magnetic losses and  $\text{MoS}_2$  provides dielectric losses, the combination of the two materials improves electromagnetic wave attenuation. This combination increases electromagnetic wave absorption and reflection, increasing the total efficacy of shielding.

Furthermore, the ability to achieve 29 dB of shielding through absorption across a broad frequency range positions this nanomaterial as a leading candidate for advanced EMI shielding applications, providing a robust solution to electromagnetic pollution in increasingly congested

electromagnetic environments [49]. In addition to its impressive absorption capabilities, the NiFe<sub>2</sub>O<sub>4</sub>@MoS<sub>2</sub> nanomaterial exhibits notable electromagnetic interference (EMI) shielding effectiveness through reflection, achieving 2.1 dBs at a higher frequency range with a material thickness of just 3 mm as shown in Fig. 9 (b). This modest yet significant reflective shielding effectiveness (SE) highlights the material's ability to deflect incident electromagnetic waves, contributing to overall EMI mitigation. The reflective properties stem from the high electrical conductivity and magnetic permeability of the NiFe<sub>2</sub>O<sub>4</sub> cores, which create impedance mismatches at the material's surface, causing incident electromagnetic waves to be reflected [50].

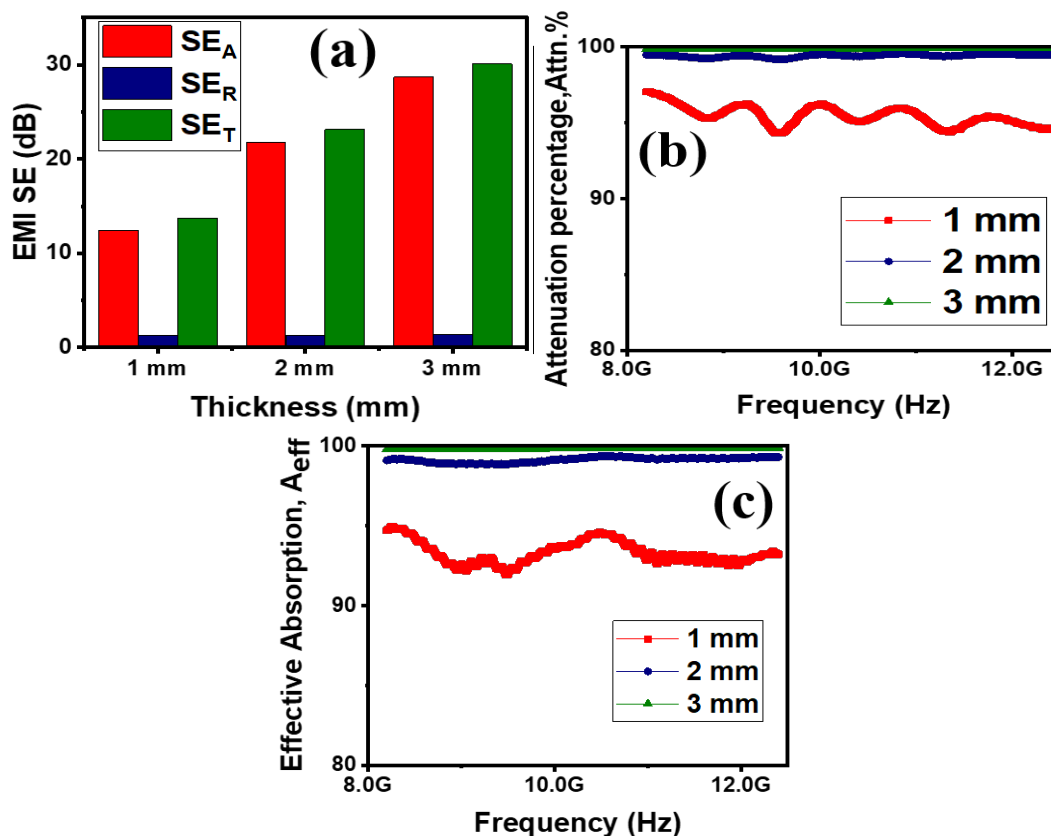


Fig. 10. (a) Histogram analysis of total shielding effectiveness, (b) attenuation percentage (c) effective absorption.

The NiFe<sub>2</sub>O<sub>4</sub>@MoS<sub>2</sub> nanomaterial showcases the total electromagnetic interference (EMI) shielding effectiveness of 30.6 dBs at higher frequencies around 11GHz with a thickness of 3 mm as shown in Fig. 9(c). This notable performance is a result of the synergistic contributions of both absorption and reflection mechanisms. The composite's flower-like structure, characterized by high surface area and intricate hierarchical architecture, plays a pivotal role in maximizing shielding effectiveness. Absorption dominates the shielding effectiveness, accounting for 29.6 dBs. This is facilitated by the interplay between the magnetic NiFe<sub>2</sub>O<sub>4</sub> cores and the dielectric MoS<sub>2</sub> layers. The NiFe<sub>2</sub>O<sub>4</sub> provides magnetic losses through natural resonance and eddy current effects, while the MoS<sub>2</sub> contributes dielectric losses via interfacial polarization and dipole relaxation. These combined mechanisms ensure efficient dissipation of electromagnetic energy as heat, significantly reducing the transmitted waves.

The histogram analysis of the NiFe<sub>2</sub>O<sub>4</sub>@MoS<sub>2</sub> nanomaterial's shielding effectiveness across the x-band (8-12 GHz) reveals insightful trends in absorption, reflection, and total shielding performance for varying thicknesses of 3 mm, 2 mm, and 1 mm as shown in Fig. 10 (a). At a thickness of 3 mm, the composite achieves a remarkable total shielding effectiveness of 30.6 dBs, with

absorption contributing 29 dBs and reflection accounting for 2.1 dBs. This high level of shielding effectiveness underscores the composite's efficiency in both dissipating and deflecting electromagnetic waves. As the thickness decreases to 2 mm, the histogram indicates a slight reduction in total shielding effectiveness, yet the material continues to perform admirably. The absorption effectiveness remains the dominant mechanism, albeit with a minor decrease, while the reflection component remains relatively stable [51]. This consistency highlights the material's robust design and its ability to maintain substantial EMI shielding despite a reduced thickness. At 1 mm, the total shielding effectiveness shows a more pronounced decrease, yet the composite still demonstrates significant EMI attenuation. The absorption effectiveness, while lower than at greater thicknesses, still provides the majority of the shielding, complemented by a consistent level of reflection. This indicates that even at minimal thickness, the NiFe<sub>2</sub>O<sub>4</sub>@MoS<sub>2</sub> nanomaterial retains its multifunctional shielding properties, making it suitable for ultra-thin applications where space and weight are critical constraints [52].

The NiFe<sub>2</sub>O<sub>4</sub>@MoS<sub>2</sub> nanomaterial demonstrates extraordinary attenuation and effective absorption capabilities across the x-band (8-12 GHz), with attenuation percentages reaching 99.9% and effective absorption at 99.7 % for thicknesses of 3 mm as shown in Fig. 10 (a,b). These values underscore the material's exceptional performance in mitigating electromagnetic interference (EMI) through both absorption and reflection mechanisms [53]. At a thickness of 3 mm, the composite achieves near-perfect attenuation and absorption, effectively neutralizing nearly all incident electromagnetic waves. This impressive performance is a result of the synergistic interplay between the NiFe<sub>2</sub>O<sub>4</sub> cores and the MoS<sub>2</sub> layers. The magnetic NiFe<sub>2</sub>O<sub>4</sub> enhances magnetic losses, while the MoS<sub>2</sub> layers contribute significantly to dielectric losses, ensuring that the composite can absorb and dissipate electromagnetic energy efficiently [54]. This outstanding performance across various thicknesses emphasizes its suitability for a wide range of high-performance EMI shielding applications, from bulky installations to ultra-thin, space-efficient electronic devices. The material's adaptability and superior shielding capabilities position it as a groundbreaking solution in the field of electromagnetic interference protection [55].

#### 4. Conclusion

A two-step synthesis technique is used for the preparation of the NiFe<sub>2</sub>O<sub>4</sub>@MoS<sub>2</sub> nanomaterial, focusing on its dynamic electrical properties across a temperature range of 183 K to 373 K. The intricate morphology of the synthesized NiFe<sub>2</sub>O<sub>4</sub>@MoS<sub>2</sub> nanomaterial is vividly revealed through (SEM). XRD analysis is led to elucidate the crystalline structure and phase integrity of the synthesized NiFe<sub>2</sub>O<sub>4</sub>@MoS<sub>2</sub> nanomaterial. The impedance plot demonstrates a transition from resistive to capacitive behavior, while the modulus plot highlights the material's bulk dielectric relaxation processes. The Bode plot of the imaginary part of impedance ( $Z''$ ) shows a peak corresponding to the relaxation frequency, shifting with temperature changes, indicating thermally activated dynamics. Conductivity versus frequency analysis reveals low values at low frequencies, increasing with frequency due to enhanced charge carrier mobility. This behavior, influenced by temperature, aligns with the small polaron hopping model. The conductivity stabilizes at higher frequencies, showcasing the material's robustness under rapid electric field oscillations. The synergistic interaction between NiFe<sub>2</sub>O<sub>4</sub> and MoS<sub>2</sub> components results in balanced electrical properties, making the nanomaterial suitable for high-performance electronic applications. The NiFe<sub>2</sub>O<sub>4</sub>@MoS<sub>2</sub> nanomaterial exhibits electromagnetic interference (EMI) shielding effectiveness primarily due to absorption, achieving a total shielding effectiveness of 30.6 dB at higher frequencies around 11 GHz.

#### Funding

Researchers supporting the project (RSP2025R118) at King Saud University.

## Acknowledgments

The authors extend their appreciation to the Researchers Supporting Project number (RSP2025R118) of King Saud University, Riyadh, Saudi Arabia.

## Competing interest

The authors have no significant financial or non-financial benefits to disclose.

## Data availability

Supporting data correlated to this manuscript will be available if mandatory

## Authors contributions

The original draft of this publication was conceptualized, synthesized, characterized, and written up in part by Ujala Anwar. Dr. Muhammad Rafi and Dr. Sohail Mumtaz helped with the experimentation, and editing of the paper, while Dr. Naveed A. Noor and Dr. Hosam O. Elansary helped with the final review, editing, and resource gathering.

## References

- [1] G. Mustafa, M. Khalid, A. Dad, C. Kiran, S. Zaheer, J. Sol-Gel Sci. Technol., 2020; <https://doi.org/10.1007/s10971-020-05359-z>
- [2] A. R. B. Bayantong, Y. Shih, C. Dong, S. Garcia-segura, M. D. G. De Luna, Nickel ferrite nanoenabled graphene oxide ( NiFe<sub>2</sub>O<sub>4</sub> @ GO ) as photoactive nanocomposites for water treatment, 2020; <https://doi.org/10.1007/s11356-020-10545-1>
- [3] M. F. Shakir et al., SN Appl. Sci., 2020; <https://doi.org/10.1007/s42452-020-2535-4>
- [4] P. Annie Vinosha, S. Deepapriya, J. D. Rodney, S. Krishnan, S. Jerome Das, J. Nanosci. Nanotechnol., vol. 19, no. 12, pp. 8020-8035, 2019; <https://doi.org/10.1166/jnn.2019.16864>
- [5] S. Atiq, M. Majeed, A. Ahmad, K. Abbas, M. Saleem, S. Riaz, Ceram. Int., 2016; <https://doi.org/10.1016/j.ceramint.2016.11.046>
- [6] D. Chen, Y. Zhang, Sci. China Technol. Sci., vol. 55, no. 6, pp. 1535-1538, 2012; <https://doi.org/10.1007/s11431-012-4772-2>
- [7] S. V. Dravid, S. D. Bhosale, S. Datar, R. K. Goyal, Nickel Nanoparticle-Filled High-Performance Polymeric Nanocomposites for EMI Shielding Applications, 2019; <https://doi.org/10.1007/s11664-019-07535-6>
- [8] U. Anwar, N.A. Noor, S. Mumtaz, I.M. Moussa, Chalcogenide Lett., vol. 22, no. 3, pp. 261-276, 2025; <https://doi.org/10.15251/CL.2025.223.261>
- [9] W. Fu, X. Xu, W. Wang, M. Ye, J. Shen, In-situ growth of NiFe<sub>2</sub>O<sub>4</sub> / 2D MoS<sub>2</sub> p-n heterojunction immobilizing palladium nanoparticles for enhanced visible-light photocatalytic activities, 2018; <https://doi.org/10.1021/acssuschemeng.8b01299>
- [10] R. B. Kamble et al., Domain size correlated magnetic properties and electrical impedance of size dependent nickel ferrite nanoparticles Domain size correlated magnetic properties and electrical impedance of size dependent nickel ferrite nanoparticles, vol. 017119, pp. 0-13, 2015; <https://doi.org/10.1063/1.4906101>
- [11] W. A. Khoso, N. Haleem, M. A. Baig, Y. Jamal, Sci. Rep., pp. 1-10, 2021; <https://doi.org/10.1038/s41598-021-83363-1>

- [12] Y. A. Mirgorod, N. A. Borshch, V. M. Fedosyuk, G. Y. Yurkov, Magnetic Properties of Nickel Ferrite Nanoparticles, vol. 49, no. 1, pp. 1375-1380, 2013; <https://doi.org/10.1134/S0020168512110064>
- [13] C. S. Erhardt, L. E. Caldeira, J. Venturini, S. R. Bragança, C. P. Bergmann, Ceram. Int., vol. 46, no. 8, pp. 12759-12766, 2020; <https://doi.org/10.1016/j.ceramint.2020.02.044>
- [14] S. Sagadevan, Z. Z. Chowdhury, R. F. Rafique, N. Brunswick, Results and Discussion," vol. 21, no. 2, pp. 21-25, 2018; <https://doi.org/10.1590/1980-5373-mr-2016-0533>
- [15] M. V. S. Kumar, G. J. S. E. Melagiriyyappa, K. K. N. H. S. Jayanna, J. Mater. Sci. Mater. Electron., vol. 29, no. 15, pp. 12795-12803, 2018; <https://doi.org/10.1007/s10854-018-9398-0>
- [16] Z. Tong et al., Carbon N. Y., vol. 179, pp. 646-654, 2021; <https://doi.org/10.1016/j.carbon.2021.04.051>
- [17] A. P. Guo, X. J. Zhang, S. W. Wang, J. Q. Zhu, L. Yang, G. S. Wang, Chempluschem, vol. 81, no. 12, pp. 1305-1311, 2016; <https://doi.org/10.1002/cplu.201600370>
- [18] F. Niu et al., Chem. Eng. J., vol. 453, no. P2, p. 139933, 2023; <https://doi.org/10.1016/j.cej.2022.139933>
- [19] Z. Masoumi et al., ACS Appl. Mater. Interfaces, vol. 13, no. 33, pp. 39215-39229, 2021; <https://doi.org/10.1021/acsami.1c08139>
- [20] P. Sivakumar, R. Ramesh, A. Ramanand, S. Ponnusamy, C. Muthamizhchelvan, Mater. Res. Bull., vol. 46, no. 12, pp. 2208-2211, 2011; <https://doi.org/10.1016/j.materresbull.2011.09.009>
- [21] A. Soam, R. Kumar, K. Sahoo, C. Mahender, B. Kumar, Synthesis of Nickel Ferrite Nanoparticles Supported on Graphene Nanosheets as Composite Electrodes for High Performance Supercapacitor, pp. 9952-9958, 2019; <https://doi.org/10.1002/slct.201901117>
- [22] N. A. Noor, U. Anwar, A. Mahmood, Chem. Phys. Lett., vol. 739, no. December 2019, p. 137031, 2020; <https://doi.org/10.1016/j.cplett.2019.137031>
- [23] M. Sangmanee, S. Maensiri, Appl. Phys. A Mater. Sci. Process., vol. 97, no. 1, pp. 167-177, 2009; <https://doi.org/10.1007/s00339-009-5256-5>
- [24] H. V. Hussain et al., Met., vol. 268, no. May, pp. 1-9, 2020; <https://doi.org/10.1016/j.synthmet.2020.116507>
- [25] Y. Shen et al., Ceram. Int., vol. 46, no. 9, pp. 13397-13406, 2020; <https://doi.org/10.1016/j.ceramint.2020.02.121>
- [26] M. Science-poland, T. T. Singh, Synthesis and study of structural properties of Sn doped ZnO nanoparticles, vol. 34, no. 3, pp. 741-746, 2016; <https://doi.org/10.1515/msp-2016-0109>
- [27] P. Mallick, N. C. Mishra, Am. J. Mater. Sci., vol. 2, no. 3, pp. 66-71, 2012; <https://doi.org/10.5923/j.materials.20120203.06>
- [28] U. Anwar et al., Mater. Today Commun., vol. 39, no. April, p. 109023, 2024; <https://doi.org/10.1016/j.mtcomm.2024.109023>
- [29] A. Chaudhuri et al., Structural and Magnetic Properties of Nickel Ferrite Nanoparticles Prepared by Solution Combustion Method Structural and Magnetic Properties of Nickel Ferrite Nanoparticles Prepared by Solution Combustion Method; <https://doi.org/10.1088/1742-6596/1644/1/012005>
- [30] M. Rafi, U. Anwar, M. H. Alnasir, A. Ramzan, A. Noor, S. Mumtaz, Ceram. Int., no. April, 2024; <https://doi.org/10.1016/j.ceramint.2024.07.229>
- [31] J. A. Lee, S. Hwang, J. Kwak, S. Il Park, S. S. Lee, K. C. Lee, Sensors Actuators, B Chem., vol. 129, no. 1, pp. 372-379, 2008; <https://doi.org/10.1016/j.snb.2007.08.034>
- [32] P. Liu, Y. Huang, J. Yan, Y. Zhao, J. Mater. Chem. C, vol. 4, no. 26, pp. 6362-6370, 2016; <https://doi.org/10.1039/C6TC01718E>
- [33] G. Nurk et al., J. Power Sources, vol. 378, no. October 2017, pp. 589-596, 2018; <https://doi.org/10.1016/j.jpowsour.2017.12.080>
- [34] V. M.-W. Huang, V. Vivier, I. Frateur, M. E. Orazem, B. Tribollet, J. Electrochem. Soc., vol. 154, no. 2, p. C89, 2007; <https://doi.org/10.1149/1.2398889>

- [35] S. T. Navale, G. D. Khuspe, M. A. Chougule, V. B. Patil, *Org. Electron.*, vol. 15, no. 10, pp. 2159-2167, 2014; <https://doi.org/10.1016/j.orgel.2014.06.019>
- [36] J. K. Jung, Y. Il Moon, G. H. Kim, N. H. Tak, *Characterization of Dielectric Relaxation Process by Impedance Spectroscopy for Polymers : Nitrile Butadiene Rubber and Ethylene Propylene Diene Monomer*, vol. 2020, 2020; <https://doi.org/10.1155/2020/8815492>
- [37] A. B. Abou Hammad, A. G. Darwish, A. M. El Nahrawy, *Appl. Phys. A Mater. Sci. Process.*, vol. 126, no. 7, pp. 1-12, 2020; <https://doi.org/10.1007/s00339-020-03679-z>
- [38] S. Chauhan, M. Kumar, S. Chhoker, S. C. Katyal, *J. Alloys Compd.*, vol. 666, pp. 454-467, 2016; <https://doi.org/10.1016/j.jallcom.2016.01.116>
- [39] J. Bisquert, G. Garcia-Belmonte, *Russ. J. Electrochem.*, vol. 40, no. 3, pp. 352-358, 2004; <https://doi.org/10.1023/B:RUEL.0000019676.99599.bc>
- [40] D. Vanidha, A. Arunkumar, S. Rajagopan, R. Kannan, *J. Supercond. Nov. Magn.*, vol. 26, no. 1, pp. 173-182, 2013; <https://doi.org/10.1007/s10948-012-1705-z>
- [41] S. Tsukamoto, V. Caciuc, N. Atodiresei, S. Blügel, *New J. Phys.*, vol. 22, no. 6, 2020; <https://doi.org/10.1088/1367-2630/ab8cac>
- [42] B. Hirschorn, M. E. Orazem, B. Tribollet, V. Vivier, I. Frateur, M. Musiani, *J. Electrochem. Soc.*, vol. 157, no. 12, p. C458, 2010; <https://doi.org/10.1149/1.3499565>
- [43] S. Manna, K. Dutta, S. K. De, *J. Phys. D. Appl. Phys.*, vol. 41, no. 15, 2008; <https://doi.org/10.1088/0022-3727/41/15/155416>
- [44] O. Farooq, M. Anis-Ur-Rehman, A. Ul Haq, *Mater. Res. Express*, vol. 7, no. 1, pp. 0-9, 2020; <https://doi.org/10.1088/2053-1591/ab5536>
- [45] Y. Zhang, Z. Yang, Y. Yu, B. Wen, Y. Liu, M. Qiu, *ACS Appl. Polym. Mater.*, vol. 1, no. 4, pp. 737-745, 2019; <https://doi.org/10.1021/acsapm.8b00025>
- [46] D. Chahar, S. Taneja, P. Thakur, A. Thakur, *J. Alloys Compd.*, vol. 843, p. 155681, 2020; <https://doi.org/10.1016/j.jallcom.2020.155681>
- [47] H. He, *Metal oxide semiconductors and conductors*. Elsevier Inc., 2020; <https://doi.org/10.1016/B978-0-12-814930-0.00002-5>
- [48] N. Yousefi et al., *Adv. Mater.*, vol. 26, no. 31, pp. 5480-5487, 2014; <https://doi.org/10.1002/adma.201305293>
- [49] S. Varshney, S. K. Dhawan, *Microw. Mater. Appl.*, pp. 575-602, 2017; <https://doi.org/10.1002/9781119208549.ch13>
- [50] Y. Zhang et al., *Compos. Part A Appl. Sci. Manuf.*, vol. 137, no. February, p. 105994, 2020; <https://doi.org/10.1016/j.compositesa.2020.105994>
- [51] M. M. Ismail, S. N. Rafeeq, J. M. A. Sulaiman, A. Mandal, *Appl. Phys. A Mater. Sci. Process.*, vol. 124, no. 5, p. 0, 2018; <https://doi.org/10.1007/s00339-018-1808-x>
- [52] C. Wan, J. Li, *Carbohydr. Polym.*, vol. 161, pp. 158-165, 2017; <https://doi.org/10.1016/j.carbpol.2017.01.003>
- [53] Y. Cheng, W. Zhu, X. Lu, C. Wang, *Compos. Commun.*, vol. 27, no. April, p. 100823, 2021; <https://doi.org/10.1016/j.coco.2021.100823>
- [54] F. Mederos-Henry et al., *Nanomaterials*, vol. 9, no. 9, 2019; <https://doi.org/10.3390/nano9091196>
- [55] H. S. Ahmad, T. Hussain, Y. Nawab, S. Salamat, *Int. J. Polym. Sci.*, vol. 2022, 2022; <https://doi.org/10.1155/2022/5952450>